Volume 18
Number 21
4 June 2026
Pages 10993-11576

Nanoscale

rsc.li/nanoscale

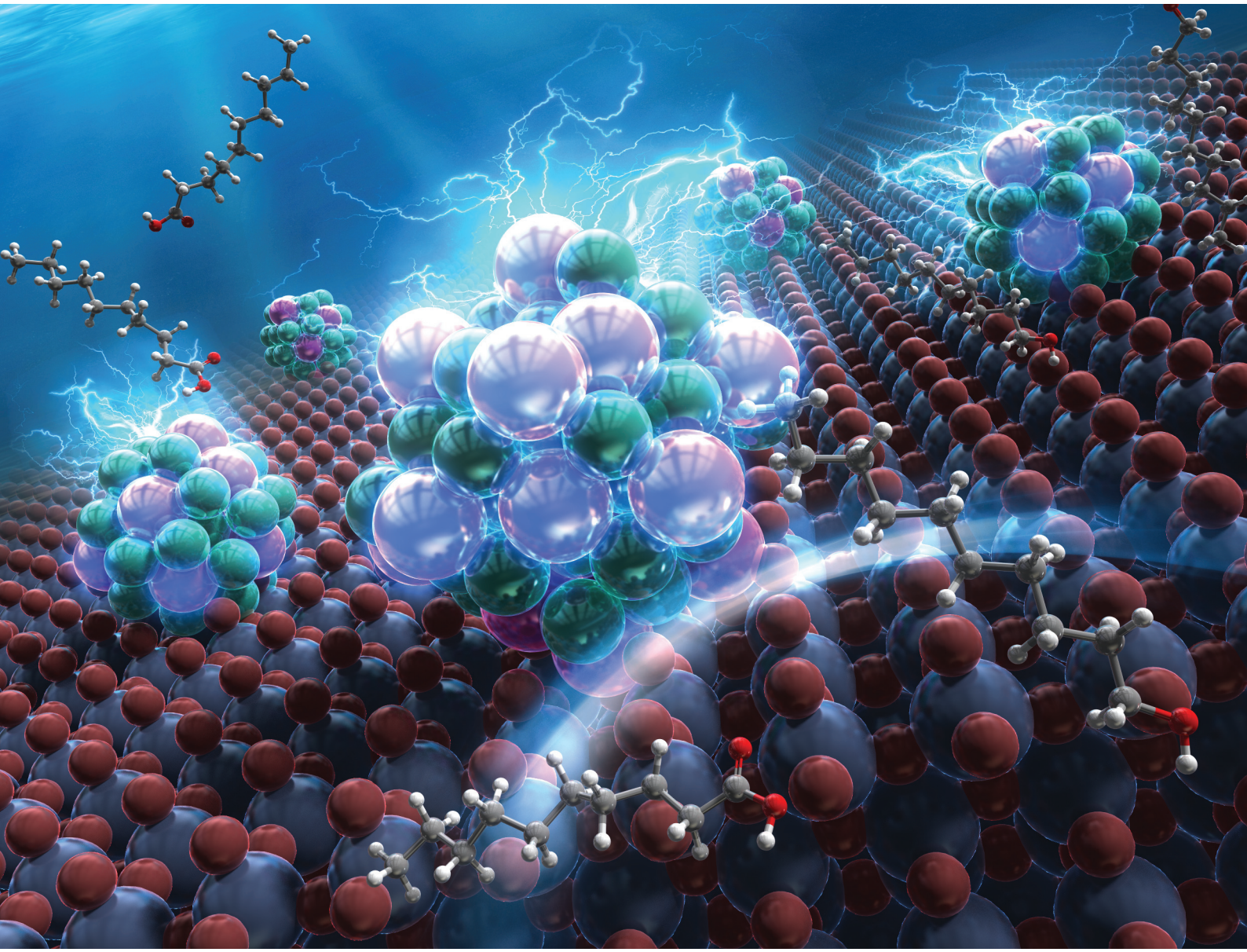

ISSN 2040-3372

ROYAL SOCIETY OF CHEMISTRY

PAPER
Masahiko Shimizu, Kazutaka Mitsuishi, Ayako Hashimoto *et al.*
Atomic-scale elucidation of formation and structure in high-performance Re–Ge nanocatalysts

NCNST

Nanoscale

PAPER

View Article Online
View Journal | View Issue

Cite this: *Nanoscale*, 2026, **18**, 11232

Atomic-scale elucidation of formation and structure in high-performance Re–Ge nanocatalysts

Masahiko Shimizu, *[a,b,c] Yuta Inami, [a] Ryuichi Shimogawa, [a,d] Takeshi Matsuo, [a] Yu Fujikata, [a] Hajime Matsumoto, [a,b] Kazutaka Mitsuishi *[e] and Ayako Hashimoto *[b,c]

Received 23rd December 2025,
Accepted 11th April 2026

DOI: 10.1039/d5nr05414a

rsc.li/nanoscale

Rational design of high-performance bimetallic nanocatalysts requires an understanding of the unique atomic structures governing their performance. This study focused on the Re–Ge/TiO_2 catalyst, which exhibits high performance for carboxylic acid hydrogenation. We analyzed structural and electronic state changes occurring during its multistep preparation involving calcination in air, hydrogen reduction, and oxidative stabilization to elucidate the key structural factors responsible for its high performance. To this end, a complementary approach combining *in situ* X-ray absorption fine structure analysis and *ex situ* scanning transmission electron microscopy (STEM) was employed. In particular, the STEM measurements utilized an air-free transfer holder to track the same individual nanoparticles throughout all preparation steps, thereby addressing two issues: the challenge of distinguishing true structural changes from particle-to-particle variations among different particles and electron beam damage associated with long exposure times. It was revealed that the highly active catalytic state after hydrogen reduction is associated with approximately 1 nm crystalline Re–Ge alloy nanoparticles. The crystal structure of the nanoparticles was a unique, low-energy, and face-centered cubic fragment, verified by density functional theory calculations. Furthermore, quantitative STEM image analysis demonstrated that the nanoparticles formed a Re–Ge random alloy. This atomic-level mixing, as detected by the spatially averaged X-ray absorption, is considered to stabilize the metallic Re(0) state, rendering Re electron-rich. These findings not only provide a new strategy for designing high-performance nanocatalysts but also establish a correlative methodology as a way to identify performance-determining factors in complex nanomaterials.

Introduction

Bimetallic nanoparticles are critically important in the design of next-generation functional materials. They exhibit unique properties attributed to interactions between constituent elements.[1,2] This strategy is particularly powerful for catalysis, where combinations of different elements can precisely control activity and selectivity at the atomic level *via* geometric and electronic effects.[3,4] Rhenium (Re) is a crucial catalytic element exhibiting excellent activity in various hydrogenation reactions.[5–10] To enhance its performance, functional optimization through combinations with other elements is essential. Indeed, alloying Re with elements such as Pd, Pt, Ru, Fe, and Ni has been reported to improve catalytic activity.[11–15]

We recently developed a novel nanocatalyst by combining Re with germanium (Ge).[16,17] It exhibits higher selectivity in direct hydrogenation of carboxylic acids compared with monometallic Re catalysts and has high activity and selectivity comparable to commercial Ru–Pt–Sn catalysts.[18] Furthermore, its precious-metal-free composition and low-cost preparation make it a promising candidate for industrial applications. However, the atomic-level structural and electronic origins of this performance enhancement remain unclear. Understanding these factors is essential for further enhancements and for rational design of next-generation nanomaterials. This requires accurately tracking atomic-level structural changes throughout multistep thermal treatments during catalyst preparation, which is difficult to achieve with conventional methods. For example, *in situ* X-ray techniques provide spatially averaged information under reaction conditions[18,19] but do not resolve the local structures of individual active sites.[20,21] Atomic-resolution scanning transmission electron microscopy (STEM) enables local structural analysis.[22–26]

[a]*Science & Innovation Center, Mitsubishi Chemical Corporation, 1000 Kamoshida-cho, Aoba-ku, Yokohama, Kanagawa, Japan.*
E-mail: masahiko.shimizu.ma@mcgc.com
[b]*Research Center for Energy and Environmental Materials, National Institute for Materials Science, 1-2-1 Sengen, Tsukuba, Ibaraki, Japan.*
E-mail: hashimoto.ayako@nims.go.jp
[c]*Graduate School of Science and Technology, University of Tsukuba, 1-2-1 Sengen, Tsukuba, Ibaraki, Japan*
[d]*Department of Materials Science and Chemical Engineering, Stony Brook University, Stony Brook, New York 11794, USA*
[e]*Center for Basic Research on Materials, National Institute for Materials Science, 1-2-1 Sengen, Tsukuba, Ibaraki, Japan. E-mail: mitsuishi.kazutaka@nims.go.jp*

However, since structural changes associated with each preparation step are typically assessed by observing different samples, the effects of sample inhomogeneity—such as variations in particle size and shape—cannot be excluded. Therefore, it is challenging to distinguish whether observed structural differences originate from changes during the catalyst preparation or reflect simply particle-to-particle variations. Although *in situ* STEM enables dynamic imaging, prolonged electron beam exposure can cause significant beam damage to the sample.[27,28]

We addressed these challenges through a complementary multi-scale approach. Using *in situ* X-ray absorption fine structure (XAFS) analysis, we tracked the spatially averaged chemical state changes across the entire sample. We then used *ex situ* STEM with an air-free transfer holder to directly image the corresponding structural changes of individual nanoparticles at the atomic scale. This approach enabled us to elucidate the changes that occur in both the structural and electronic states occurring during each preparation step of Re–Ge catalysts and to identify the key structural factors responsible for the high performance. Unique crystalline nanoparticles of approximately 1 nm in diameter were observed in their highly active state after hydrogen reduction. Furthermore, XAFS analysis indicated that Re–Ge alloy formation stabilized the metallic Re(0) state, rendering Re electron-rich. These results not only confirm a new strategy for designing high-performance nanocatalysts but also demonstrate an effective analytical methodology for the structural analysis of various complex nanomaterials.

Materials and methods

Sample preparation

The TiO_2-supported Re–Ge catalyst (Re–Ge/TiO_2) was prepared with a co-impregnation method that was previously reported.[17] An aqueous solution of NH_4ReO_4 and GeO_2 impregnated the support; this was followed by drying and calcination in air at 300 °C. The nominal loadings of Re and Ge were 5 wt% and 3 wt%, respectively. A portion of this calcined powder was directly used for *in situ* XAFS measurements and as the starting material for *ex situ* STEM imaging. To analyze the reduced catalyst, another portion of the powder was exposed to hydrogen at 500 °C. The reduced sample was then stored in an argon-filled glove box.

X-ray diffraction analysis

Powder X-ray diffraction (XRD) patterns of TiO_2 and the hydrogen-reduced Re–Ge/TiO_2 catalyst were recorded using a diffractometer (D8 Advance, Bruker AXS) with Cu Kα radiation (40 kV, 40 mA). Data were collected over a 2θ range of 15–90° with a step size of 0.02°. To prevent exposure to air during the measurement, the sample was sealed in a Si-based airtight holder filled with argon.

For the calcined and oxidized Re–Ge/TiO_2 catalysts, powder XRD patterns were re-measured using a diffractometer (Empyrean, Malvern Panalytical) with Cu Kα radiation (45 kV, 40 mA) in reflection mode. Data were collected over a 2θ range of 10–80° with a step size of 0.008°. Each sample was measured by four repeated scans.

In situ XAFS measurement

XAFS measurements were performed at the BL-9C beamline of the Photon Factory at KEK (Tsukuba, Japan). Re L_3 edge (10 535 eV) and Ge K edge (11 103 eV) spectra were obtained in transmission mode. *In situ* measurements were performed using an electric furnace cell equipped with an automated gas mixing system. The Re–Ge/TiO_2 or Re/TiO_2 sample was loaded into the cell, and spectra were first recorded in air. The sample was then reduced under flowing hydrogen as the temperature was increased from room temperature to 500 °C at 10 °C min^{-1}. XAFS spectra were recorded continuously during the temperature ramp. After holding it at 500 °C, the sample was then cooled to 50 °C under hydrogen. The gas atmosphere was then switched sequentially from H_2 to N_2, 5% O_2/N_2, and 20% O_2/N_2 at 50 °C to investigate the oxidation behavior. For comparison, Re/TiO_2 (without Ge) was analyzed under identical conditions.

XAFS data processing was performed with the Larch software package.[29] Energy calibration was conducted using Re and Ge metal references, where the edge energy (E_0) was defined as the first zero-crossing point of the second derivative of the absorption spectrum. This was 10 535 eV for the Re L_3 edge and 11 103 eV for the Ge K edge. Extended XAFS (EXAFS) fitting was performed in *R*-space with FEFF8.5L software bundled with Larch. Details of the fitting procedure are provided in the SI.

Ex situ STEM observation

Prior to sample loading, multiple 2 μm-diameter pores were created in the heating silicon nitride membrane of the microelectromechanical chip (Hummingbird Scientific) using a gallium focused ion beam (JIB-4000, JEOL) to minimize background signals from the support membrane for high-resolution STEM imaging. The Re–Ge/TiO_2 powder was then loaded onto the chip, which was subsequently mounted onto an air-free transfer TEM holder (Hummingbird Scientific). Prior to imaging, the sample surface was subjected to plasma cleaning (GV10x, Ibss Group, Inc.) to remove contaminants. All images were acquired using an aberration-corrected TEM (JEM-ARM200F, JEOL) operated at 200 kV. To minimize beam-induced changes, probe alignment (*e.g.*, focusing) was performed in a different area from the observation target, and the target nanoparticles were exposed only during image acquisition. The probe current was kept at approximately 20 pA. For *ex situ* processing, the sample mounted in the air-free holder was transferred from the TEM to a vacuum chamber. Inside the chamber, the sample was heated using the membrane chip under a sealed atmosphere of selected preparation gases at approximately 0.5 atm. The procedure consisted of hydrogen reduction (500 °C, 30 min hold), followed by oxidative stabilization (5% O_2/N_2 at room temperature). After each step, the holder was returned to the TEM without exposure to air, which allowed imaging of structural changes in the same nano-

particles. High-angle annular dark-field STEM (HAADF-STEM) images were acquired with a convergence angle of 20.8 mrad, a pixel size of 2048 × 2048, and a dwell time of 5 μs per pixel.

High-resolution STEM observation of nanoparticles after hydrogen reduction

To analyze the composition and crystal structure of the nanoparticles in their high-performance state after hydrogen reduction, high-resolution STEM images were acquired. The hydrogen-reduced Re–Ge/TiO_2 powder was handled under an inert atmosphere to prevent exposure to air. Inside an argon-filled glovebox, the powder was dispersed onto a copper TEM grid (EM Japan), which was then loaded onto an air-free transfer holder (JEOL) for insertion into an aberration-corrected TEM (JEM-ARM300F, JEOL). All imaging was performed with an acceleration voltage of 300 kV. HAADF-STEM images were acquired with a convergence semi-angle of 23.6 mrad and a collection range of 73–175 mrad. The image size and dwell time were 2048 × 2048 pixels and 5 μs per pixel, respectively. For elemental mapping, STEM combined with energy dispersive X-ray spectroscopy (STEM-EDS) was performed with an acquisition time of 300 s.

Density functional theory calculations

To examine the possible stable structures of Re nanoclusters, we performed structural optimization calculations based on those reported previously.[30] Thirty structurally different 55-atom clusters with high symmetry were used as initial structures. Their relative stabilities were evaluated by comparing their total energies after structural optimization. Density functional theory (DFT) calculations were performed with the Quantum ESPRESSO package,[31] with plane-wave basis sets and projected augmented-wave pseudopotentials.[32,33] The energy cutoff of the plane-wave basis set was 51 Ry. The exchange–correlation functionals were treated within the generalized gradient approximation using the Perdew–Burke–Ernzerhof[34] form. The finite-size clusters were placed in a cubic supercell having an edge length of 25 Å, which was sufficiently large to avoid interactions between clusters in neighboring cells. To account for the large size of the unit cells, all calculations were restricted to the Γ point of the Brillouin zone. During the geometric optimization, the convergence threshold was 10^{-6} Ry for self-consistent electronic minimization, and all atoms were allowed to relax until the forces were below 10^{-3} Ry $Å^{-1}$.

HAADF-STEM image simulation

To determine the atomic mixing pattern within the nanoparticles, HAADF-STEM image contrast simulations were performed to reproduce the experimental images. All atomic models were constructed based on the crystal structure determined from the STEM images and DFT calculations. The models were initially created as spherical clusters, with their diameters set to match the experimentally observed particle sizes, and their central coordinates were set to align with the arrangement of atomic columns in the experimental images. We then generated several atomic models for major mixing patterns, including core–shell, subcluster-segregated, ordered alloy and random alloy structures, as described previously.[1,2] The overall composition of each model was Re-rich, in accordance with STEM-EDS results. Finally, the models were cut into hemispheres to match the observed particle shape. To reproduce the intensities of each atomic column in the experimental images (as obtained by two-dimensional Gaussian fitting), the substitutional Re and Ge sites were optimized. The HAADF-STEM image simulations were performed with the multi-slice method implemented in the abTEM code.[35] All simulation parameters, including the accelerating voltage, convergence angle, and HAADF detector collection angles, were set to match the experimental conditions. Thermal vibrations were accounted for using a frozen phonon model with 100 configurations.

Results and discussion

Electronic and local structure analyses of hydrogen reduction and oxidative stabilization

The standard preparation method for the Re–Ge catalyst consists of three sequential gas-phase treatments after the impregnation of Re and Ge precursors onto the TiO_2 support: (1) calcination in air to decompose supported salts, (2) hydrogen reduction for catalyst activation, and (3) oxidative stabilization to enable safe handling in air.[17] While the Re–Ge catalyst prepared by hydrogen reduction (step 2) exhibits high hydrogenation activity and selectivity, the subsequent oxidative stabilization step (step 3) can decrease both catalytic activity and selectivity, despite being essential for safe handling at the industrial scale.[36] Understanding this deactivation mechanism and identifying the primary cause of performance loss are crucial for improving catalyst production. To elucidate the local structure and electronic state of the Re–Ge nanoparticles during these preparation steps, *in situ* XAFS measurements were performed during both the reduction and oxidative stabilization steps.

Fig. 1 shows the XAFS spectra of Re–Ge/TiO_2 at different treatment stages, while Fig. S1 shows the temperature-dependent changes in the X-ray absorption near edge structure (XANES) spectra during the reduction step. Fig. S2 presents the XANES spectra in Fig. 1 overlaid with reference compounds: Re metal, ReO_2, ReO_3, and NH_4ReO_4 for the Re L_3 edge and Ge(0) and hexagonal GeO_2 for the Ge K edge. Before reduction, the Re L_3 edge spectrum exhibited a peak position comparable with that of Re(IV), Re(VI), and Re(VII) references, confirming the presence of oxidized Re compounds (Fig. S2a). The corresponding Fourier transform spectrum (Fig. 1c) matches well with that of NH_4ReO_4 in *R* space. After hydrogen reduction at 500 °C, the white line intensity significantly decreases, and the edge position shifts to lower energy. However, the position remains higher than that of Re(0), indicating partial reduction toward the metallic state (Fig. S2a). The Fourier transform spectrum shows that the intensity of the peak corresponding to the first coordination shell decreases as the reduction proceeds (Fig. 1c).

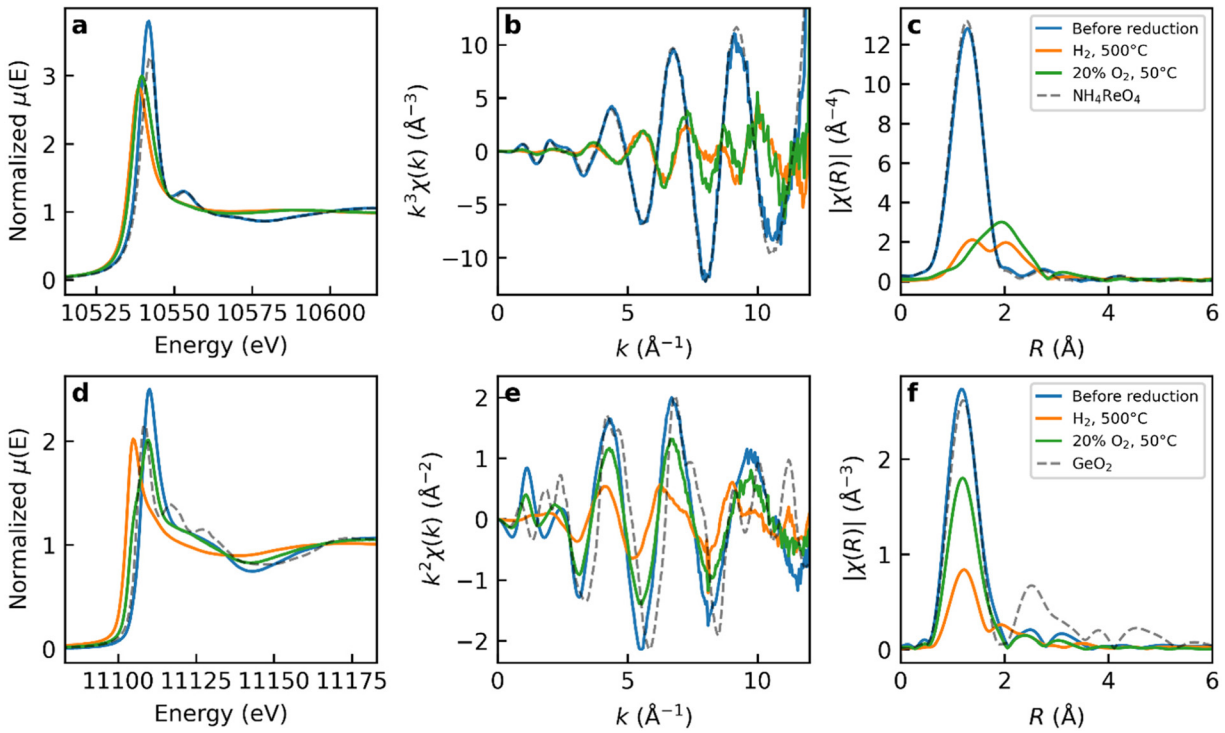

Fig. 1 X-ray absorption fine structure (XAFS) analysis of Re–Ge/TiO_2 at different treatment stages. Top row: Re L_3 edge data showing (a) X-ray absorption near edge structure (XANES), (b) k^3-weighted extended XAFS (EXAFS) oscillations, and (c) Fourier transform magnitude. The NH_4ReO_4 reference is shown as a dashed line. Bottom row: Ge K edge data showing (d) XANES, (e) k^2-weighted EXAFS oscillations, and (f) Fourier transform magnitude. Data are shown for four conditions: before reduction (blue), after hydrogen reduction at 500 °C (orange), after exposure to 20% O_2 at 50 °C (green), and the GeO_2 reference (dashed line).

Similarly, for the Ge K edge, the XANES spectrum before reduction matches well with that of GeO_2, confirming that Ge exists in the Ge(IV) oxidized state (Fig. S2b). The Fourier transform spectrum (Fig. 1f) also shows good agreement with that of GeO_2 in R space. After hydrogen reduction, the edge position shifts to lower energy, and the intensity of the first-shell peak decreases. However, the white line intensity remains higher than that of Ge(0), indicating partial reduction, as observed for Re.

The temperature-dependent XANES spectra (Fig. S1) provide insight into the reduction mechanism. For the Re L_3 edge (Fig. S1a), the absence of an isosbestic point during reduction indicates that the transformation involves more than two chemical compounds. This suggests that the reduction of Re proceeds through multiple intermediate oxidation states, from Re(VII) and/or Re(VI) through Re(IV) to Re(0), rather than through a simple two-state conversion. Such reductions involving multiple intermediate species have also been reported in the Re/TiO_2 system.[10] In contrast, the Ge K edge spectra (Fig. S1b) exhibit behavior consistent with a two-component system, suggesting that the reduction of Ge proceeds directly from Ge(IV) to Ge(0) without detectable intermediate oxidation states.

To quantitatively analyze the structural evolution during each preparation step, EXAFS curve-fitting analyses were performed, as summarized in Tables 1 and 2. Fig. 2, Tables S2 and S3 show the temperature dependences of the structural and fitting parameters during hydrogen reduction. The individual fitting results in R-space are presented in Fig. S3–S5.

A significant difference was observed in the EXAFS spectra in R-space for Re–Ge/TiO_2 and Re/TiO_2 at 500 °C under hydrogen (Fig. 3b), indicating the presence of Re–Ge bonds in the bimetallic catalyst. A two-shell fit with Re–O and Re–Ge paths reproduced the EXAFS signals, yielding a Re–Ge bond distance

Table 1 Re L_3 edge extended X-ray absorption fine structure fitting results for the Re–Ge/TiO_2 samples

Sample	Path	N	R (Å)	σ^2 ($\times 10^{-3}$ Å^2)	ΔE_0 (eV)	R-Factor	χ^2_v
Re–Ge/TiO_2 before reduction	Re–O	5.3 ± 2.7	1.775 ± 0.032	0.0 ± 1.9	7.5 ± 8.3	2.9%	557.0
Re–Ge/TiO_2 H_2 500 °C	Re–O	1.2 ± 1.4	1.899 ± 0.074	0.1 ± 11.9	−11.0 ± 12.3	4.9%	135.1
	Re–Ge	2.8 ± 3.3	2.448 ± 0.066	10.7 ± 8.8			
Re–Ge/TiO_2 O_2 50 °C	Re–O	1.3 ± 1.4	2.067 ± 0.055	0.1 ± 5.0	14.6 ± 10.0	5.4%	81.7
	Re–Ge	1.8 ± 2.3	2.554 ± 0.051	6.0 ± 10.3			

Table 2 Ge K edge extended X-ray absorption fine structure fitting results for the Re–Ge/TiO_2 samples

Sample	Path	N	R (Å)	σ^2 ($\times 10^{-3}$ Å^2)	ΔE_0 (eV)	R-Factor	χ^2_v
Re–Ge/TiO_2 before reduction	Ge–O	4.7 ± 2.2	1.729 ± 0.034	0.0 ± 5.1	−1.0 ± 7.2	5.0%	1092.0
Re–Ge/TiO_2 H_2 500 °C	Ge–O	1.5 ± 0.4	1.735 ± 0.018	0.0 ± 3.6	−10.0 ± 4.0	1.8%	29.8
	Ge–Re	3.0 ± 2.1	2.547 ± 0.029	12.7 ± 7.0			
Re–Ge/TiO_2 O_2 50 °C	Ge–O	3.2 ± 1.4	1.738 ± 0.032	0.6 ± 5.0	0.7 ± 6.6	4.6%	881.3

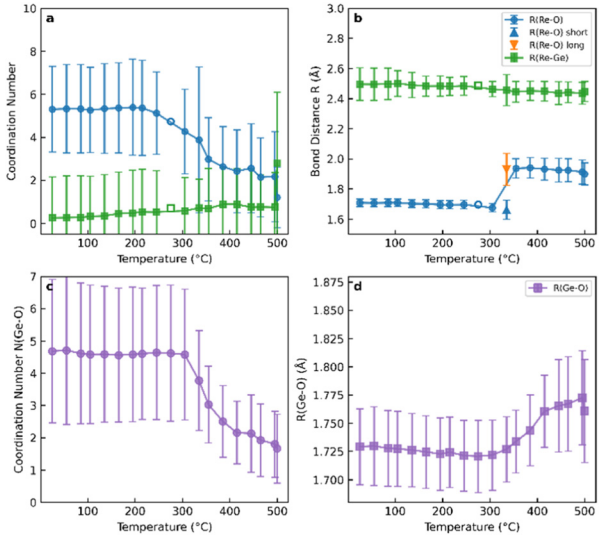

Fig. 2 Temperature dependence of extended X-ray absorption fine structure fitting parameters for Re–Ge/TiO_2 during hydrogen reduction. (a) Coordination numbers from Re L_3 edge fitting: N(Re–O) (blue circles) and N(Re–Ge) (green squares). (b) Bond distances from Re L_3 edge fitting: R(Re–O) (blue circles) and R(Re–Ge) (green squares). (c) Coordination number N(Ge–O) from Ge K edge fitting. (d) Bond distance R(Ge–O) from Ge K edge fitting. The transition at ~335 °C corresponds to the onset of Re reduction and Re–Ge alloy formation. The 500 °C data point is from the merged spectra to improve the signal-to-noise ratio.

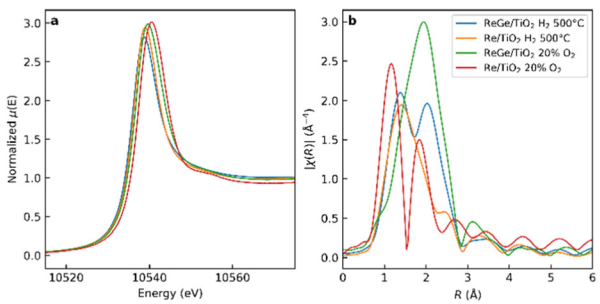

Fig. 3 Comparison of Re L_3 edge extended X-ray absorption fine structure for the Re–Ge/TiO_2 and Re/TiO_2 catalysts. (a) X-ray absorption near edge structure spectra and (b) Fourier transform magnitude. Re–Ge/TiO_2 H_2 500 °C (blue), Re/TiO_2 H_2 500 °C (orange), Re–Ge/TiO_2 20% O_2 (green), and Re/TiO_2 20% O_2 (red).

of 2.448 ± 0.066 Å, which is significantly shorter than the Re–Re bond distance reported for Re/TiO_2 [10] (2.76 ± 0.01 Å). In contrast, a two-shell fit with Re–O and Re–Re paths did not adequately reproduce the experimental data owing to the longer bond distance of the Re–Re shell.

For the Re L_3 edge (Fig. 2a and b), the Re–O coordination number, N(Re–O), and the Re–O bond distance, R(Re–O) (~1.7 Å) remain consistent with the tetrahedral ReO_4^- structure of NH_4ReO_4 below 280 °C. Above this temperature, N(Re–O) begins to decrease, indicating the onset of Re reduction. At intermediate temperatures (approximately 335 °C), EXAFS fitting required both short and long Re–O paths (Fig. S4l, Table S2), indicating the coexistence of multiple Re–O coordination environments consistent with the multi-step reduction suggested by the XANES data. Above 335 °C, the model with a long Re–O bond provided physically reasonable parameters.

Above 335 °C, N(Re–Ge) begins to increase as N(Re–O) continues to decrease, indicating the formation of Re–Ge bonds concurrently with the loss of Re–O coordination. However, owing to the strong correlation between the coordination number and the Debye–Waller factor (σ^2) in the EXAFS fitting, the error bars associated with N(Re–Ge) and σ^2(Re–Ge) are too large to allow a quantitative comparison; therefore, only a trend of increasing N(Re–Ge) can be inferred. At 500 °C, the fitting results show N(Re–Ge) = 2.8 ± 3.3 with R(Re–Ge) = 2.448 ± 0.066 Å (Table 1).

For the Ge K edge (Fig. 2c and d), N(Ge–O) and R(Ge–O) (~1.73 Å) remain consistent with those of GeO_2 below 300 °C (Fig. S5). Above this temperature, N(Ge–O) decreases similarly to Re, suggesting concurrent reduction and alloy formation. It is noteworthy that even after 500 °C reduction under hydrogen, a significant Ge–O contribution remains with N(Ge–O) = 1.5 ± 0.4 (Table 2), indicating that a substantial fraction of Ge exists as oxides on the TiO_2 support.

For the spectrum at 500 °C, fitting with a two-shell model including Ge–O and Ge–Re paths yielded N(Ge–Re) = 3.0 ± 2.1 and R(Ge–Re) = 2.547 ± 0.029 Å (Table 2). This spectrum could also be fitted with a two-shell model including Ge–O and Ge–Ge paths, yielding N(Ge–Ge) = 1.2 ± 1.3 and R(Ge–Ge) = 2.431 ± 0.033 Å (Table S1). This Ge–Ge bond distance is comparable to that in Ge bulk (2.45 Å).[37] Although the Ge–Re model provided a marginally better fit (R-factor = 1.8% *vs.* 3.3%), both structural models remain plausible given the similar fit quality, and the Ge K-edge data alone do not allow us to exclude Ge–Ge bonding. The fitted Ge–Re bond distance (2.547 Å) is slightly longer than the Re–Ge distance obtained from the Re L_3 edge analysis (2.448 Å). Nevertheless, these values are comparable within experimental uncertainty. Considering the clear Re–Ge contribution observed from the Re L_3 edge, we conclude that Ge–Re bonds are present in the reduced catalyst. However, the

Ge–Ge contribution may also be significant, suggesting that both Ge–Re and Ge–Ge coordination environments coexist in the reduced catalyst.

The XANES spectra of Re–Ge/TiO_2 and Re/TiO_2 were compared to investigate the effect of Ge addition on the electronic state of Re. Fig. S6 shows the Re L_3 edge XAFS analysis of the Re/TiO_2 catalyst at different treatment stages and Fig. 3 presents a direct comparison between Re–Ge/TiO_2 and Re/TiO_2. After hydrogen reduction at 500 °C, the Re L_3 edge XANES spectrum of Re–Ge/TiO_2 exhibits a lower white line intensity and a slight shift to lower energy compared with that of Re/TiO_2 (Fig. 3a). This decrease in white line intensity indicates that Re in the bimetallic catalyst has a higher electron density, suggesting that the formation of the Re–Ge alloy stabilizes the metallic Re(0) state more effectively than in the monometallic catalyst. This electron-rich Re is closely related to the enhanced Re–Ge catalytic performance.

The structural changes were investigated to understand the origin of the decreased catalytic performance after oxidative stabilization. Upon exposure to 20% O_2 at 50 °C, distinctly different behaviors were observed for Re–Ge/TiO_2 and Re/TiO_2 catalysts (Fig. 3). For Re/TiO_2, significant changes in both the XANES spectrum and the Fourier transform magnitude were observed after oxidation (Fig. S6), indicating substantial re-oxidation of Re(0). In contrast, Re–Ge/TiO_2 exhibited relatively minor changes in the Re L_3 edge spectra after oxidative stabilization (Fig. 1a–c), with the white line intensity remaining lower than that of Re/TiO_2 (Fig. 3a). This suggests that the Re–Ge alloy structure provides enhanced oxidation resistance when compared with Re/TiO_2.

The EXAFS fitting results (Tables 1 and 2) also support this interpretation. For the Re L_3 edge, the Re–Ge bond remains detectable after oxidative stabilization with N(Re–Ge) = 1.8 ± 2.3 and R(Re–Ge) = 2.554 ± 0.051 Å (Table 1). Although no definitive conclusion can be drawn regarding the coordination number owing to the strong N–σ^2 correlation in the fit, the persistence of the Re–Ge contribution suggests that the Re–Ge alloy structure formed at high temperature is at least partially preserved, indicating that the Re–Ge alloy layer has higher resistance to oxidation. In contrast, at the Ge K edge, the coordination number N(Ge–O) increases from 1.5 ± 0.4 (H_2, 500 °C) to 3.2 ± 1.4 (O_2, 50 °C) after oxidation (Table 2), while the second shell peak corresponding to the Ge–Re (or Ge–Ge) bonds significantly decreases in intensity (Fig. 1f, comparing the green and red curves). This indicates that the reduced Ge compounds have been substantially re-oxidized.

These observations suggest that the addition of Ge leads to the formation of a stable Re–Ge alloy layer that confers oxidation resistance, thereby stabilizing the Re(0) state. Meanwhile, most of the Ge exists as Ge–Ge-rich regions or oxide species on the support and are readily converted to GeO_2 under oxidizing conditions. The re-oxidation of Ge compounds within the alloy nanoparticles upon oxidative stabilization is expected to disrupt the atomic-level mixing of Re and Ge that characterizes the active state. This would potentially lead to structural degradation of the nanoparticles.

Observation of structural changes during catalyst preparation stages

To elucidate the structural changes corresponding to chemical state changes detected by *in situ* XAFS, further analyses were performed. First, XRD measurements were conducted on the catalyst at each preparation stages, including after calcination, after hydrogen reduction, and after oxidative stabilization (Fig. S7). In all cases, only diffraction peaks from the TiO_2 support (anatase) were observed, and no crystalline phases of Re, Ge, or their alloys were detected. Therefore, we performed *ex situ* STEM imaging to track the structural changes at each preparation step at the atomic scale. The preparation conditions (calcination in air, hydrogen reduction, and oxidative stabilization) were reproduced using the air-free transfer TEM holder combined with the vacuum chamber. This enabled tracking of the same nanoparticles throughout all preparation steps without air exposure.

Fig. 4a–c show the *ex situ* HAADF-STEM images of the same field of view at each preparation step. After calcination in air (Fig. 4a), both Re and Ge species were found to be highly dispersed on the TiO_2 support, primarily as sub-nanometer clusters and some individual atoms. In contrast, nanoparticles were formed after hydrogen reduction (Fig. 4b). The particle size distribution of approximately 700 particles, according to a reported method,[38] yielded an average diameter of 1.3 ± 0.3 nm (see the histogram in Fig. S8). The nanoparticles remain clearly visible after the oxidative stabilization step (Fig. 4c), with no observable changes in their size or position. These observations directly demonstrate that approximately 1 nm nanoparticles are formed from the dispersed species during hydrogen reduction. Furthermore, their size and position on the support remain unchanged at the atomic scale during oxidation stabilization. Fig. 4d and e show the HAADF-STEM images of the same particle after hydrogen reduction and after oxidation stabilization, respectively. The highly active particles after hydrogen reduction exhibit lattice fringes. In contrast, the fringes disappear for the low-activity particles after oxidative stabilization. This loss of crystallinity was also confirmed by the disappearance of the diffraction spots from the nanoparticles in the corresponding fast Fourier transform (FFT) images (Fig. 4f and g and Fig. S9). Under our imaging conditions, control electron beam irradiation experiments confirmed that these crystallization/amorphization changes were not beam-induced but resulted from the respective preparation steps (Fig. S10).

The Re–Ge/TiO_2 catalytic performance differs between the post-hydrogen-reduction state (high activity and selectivity) and the post-oxidative stabilization state (low activity and selectivity).[36] The results shown in Fig. 4b and c indicate that this performance decline cannot be explained by the changes in particle size or dispersion. Therefore, the loss of nanoparticle crystallinity, revealed in Fig. 4d–g, is likely the primary cause of catalyst deactivation. This is consistent with the *in situ* XAFS results, which showed that Ge in the nanoparticles was re-oxidized upon oxygen exposure, as evidenced by the increased Ge–O coordination number and decreased Ge–Re

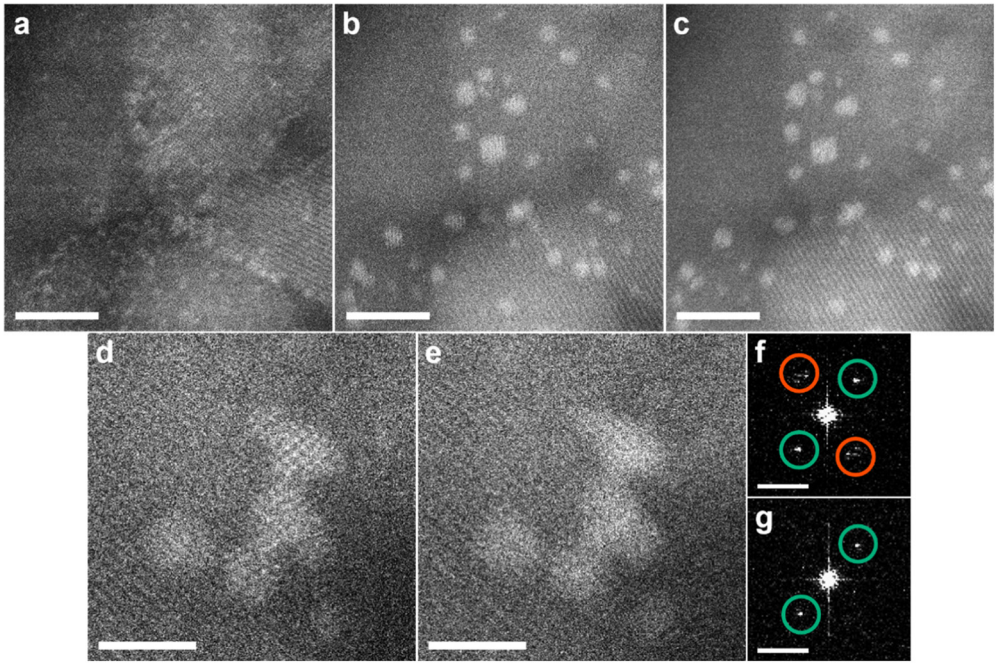

Fig. 4 *Ex situ* high-angle annular dark-field scanning transmission electron microscopy images of the Re–Ge/TiO_2 catalyst at each preparation stage. A series of images showing the same field of view after (a) calcination in air, (b) hydrogen reduction, and (c) oxidative stabilization. High-magnification images of the same nanoparticle after (d) hydrogen reduction and (e) oxidative stabilization. (f and g) Corresponding fast Fourier transform patterns obtained from the images shown in (d) and (e), respectively. The red and green circles indicate the diffraction spots from the nanoparticle and the TiO_2 support, respectively. Note that the spots from the nanoparticle are not observed in (g) after oxidative stabilization. Scale bars: 5 nm in (a–c); 2 nm in (d and e); and 5 nm^{-1} in (f and g).

contributions. This Ge oxidation disrupts the atomic-level Re–Ge mixing essential for stabilizing the metallic Re(0) state, thereby explaining both the loss of crystallinity and the accompanying decline in catalytic performance. Thus, the ability to clearly decouple multiple structural factors affecting catalytic performance was made possible by the complementary approach of combining spatially averaged XAFS with direct atomic-resolution STEM imaging.

Atomic-scale structural analysis of nanoparticles in the catalytically active state

We then investigated the atomic structure of the nanoparticles in their active state after hydrogen reduction. Re is considered to be the primary active site, while Ge serves as a co-catalyst that enhances selectivity.[16,36] If the stabilization of the metallic Re(0) state through Re–Ge alloy formation suggested by *in situ* XAFS is key to the co-catalyst effect, elucidating the atomic arrangement within the nanoparticles is crucial. Therefore, a detailed analysis of the composition, crystal structures, and atomic mixing patterns of the catalytically active nanoparticles was performed.

First, the elemental composition of the nanoparticles was investigated using STEM-EDS. Fig. 5a shows an elemental map overlaying Re M (red) and Ge L (green) maps (the individual maps for Re and Ge are shown in Fig. S11). The nanoparticles contain Re and Ge, as shown for the representative particles highlighted by the frames. Quantitative analysis of approximately 50 particles indicated that both Re and Ge were detected in every particles, with an average Ge/Re atomic ratio of 0.53 ± 0.25 (see the histogram in Fig. S12). This is consistent with the overall ratio of 0.51 obtained from the entire mapped area. The observed Ge/Re ratio is significantly lower than the nominal Ge/Re loading ratio of approximately 1.5, indicating that only a small fraction of the total loaded Ge is incorporated into the Re-Ge nanoparticle alloys. The remaining Ge most likely exists as highly dispersed GeO_x compounds on the TiO_2 support that are below the STEM-EDS detection limit. This interpretation is consistent with the substantial Ge–O coordination number detected by XAFS after hydrogen reduction. This Re-rich composition, combined with the *in situ* XAFS finding that both elements are in the metallic state, indicates that the nanoparticles are Re-based Re–Ge alloys. The formation of this Re-rich alloy is inconsistent with the bulk Re-Ge equilibrium phase diagram, where only a Ge-rich intermediate phase is considered thermodynamically stable.[39,40] Therefore, the nanoparticles exist in a nanoscale-specific metastable phase.[1]

The crystal structure of the nanoparticles was investigated based on the HAADF-STEM images. Fig. 5b shows an image acquired from an area nearly identical to that shown in Fig. 5a, while Fig. 5c is a magnified image of a representative nanoparticle selected for analysis. This particle reflects the average characteristics of the nanoparticle ensemble in terms of both size (1.5 nm in diameter) and composition (Ge/Re = 0.47). The FFT pattern obtained from the image of this particle (Fig. 5c, inset) shows hexagonal reflections. This characteristic structure

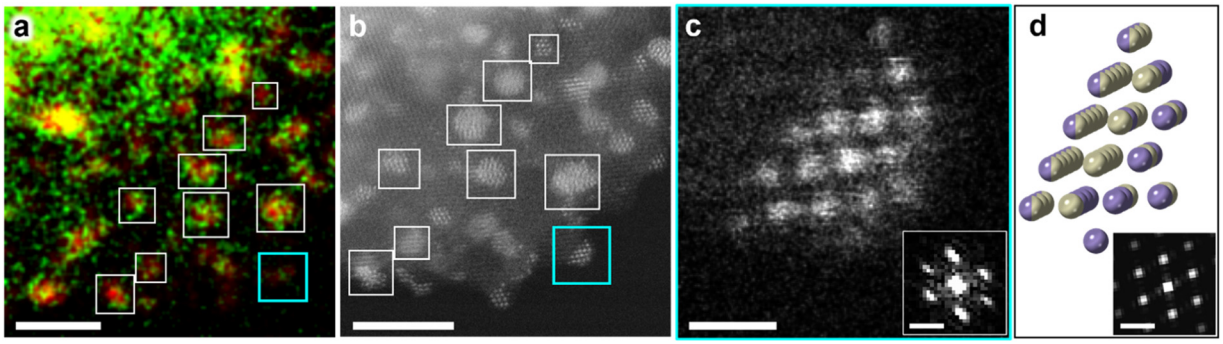

Fig. 5 Scanning transmission electron microscopy (STEM) analysis of the Re-Ge/TiO_2 nanoparticles after hydrogen reduction. (a) STEM energy dispersive X-ray spectroscopy elemental map overlaying Re M (red) and Ge L (green) maps. Representative particles are indicated by frames. (b) High-angle annular dark-field STEM (HAADF-STEM) image of an area nearly identical to (a). (c) Magnified HAADF-STEM image of the particle indicated by the sky-blue frame in (a and b) and the corresponding fast Fourier transform pattern (inset). (d) Atomic model of the Re–Ge nanoparticle based on the face-centered cubic fragment structure obtained from density functional theory calculations and a simulated diffraction pattern (inset). The model is displayed slightly tilted from the zone-axis orientation for clarity. The atom colors indicate Re (beige) and Ge (purple). Atoms whose elemental assignment was unclear owing to positional overlap with the support are displayed in both colors. Scale bars: 5 nm in (a and b); 0.5 nm in (c); and 5 nm^{-1} in the insets of (c and d).

was commonly observed among the nanoparticles of this catalyst (Fig. S13). However, the FFT pattern did not match those of the hexagonal close-packed (HCP) structure of bulk Re,[41] the diamond structure of Ge,[41] or the theoretically calculated icosahedral structure of Re nanoparticles.[30] Based on the EDS analysis indicating that this nanoparticle is Re-rich, we focused on Re-based structural models and first tested whether a distorted HCP Re structure could reproduce the experimental FFT pattern. We therefore examined anisotropically distorted HCP Re models by varying the *a*-axis strain (ε_a) and *c*-axis strain (ε_c); however, none of them could reproduce the experimental FFT patterns or the real-space atomic arrangement (Table S4 and Fig. S14). To explore alternative Re-based structural models that could explain the experimental results, DFT calculations were performed. The calculations revealed that, in addition to the previously reported icosahedral structure,[30] the face-centered cubic fragment (FCCf) structure[30,42] is also identified as a low-energy candidate (Fig. S15). Therefore, a hemispherical atomic model based on this FCCf structure was constructed, reflecting the experimentally observed particle size. Fig. 5d shows the atomic model and the corresponding simulated diffraction. This model showed good agreement with the experimental results (Fig. 5c) in both the real-space atomic arrangement (HAADF-STEM image) and the reciprocal-space diffraction pattern. It should be noted that the present DFT calculations were performed for free-standing Re clusters without explicitly considering the TiO_2 support. Although support interactions may affect cluster stability and structure, such an analysis is beyond the scope of this study.

To elucidate the atomic mixing pattern of Re and Ge within this FCCf structure, the *Z*-contrast in the HAADF-STEM images was quantitatively analyzed.[43–45] The experimental intensity profiles were compared with those simulated based on the major atomic ordering models for bimetallic nanoparticles, including core–shell, subcluster-segregated, ordered alloy and random alloy structures[1,2] (see Fig. S16). The results demonstrated that the random alloy model, in which Re and Ge are atomically mixed, as depicted in Fig. 5d, best reproduced the experimental image. This finding was consistent with the spatially averaged XAFS results, which indicated that Re and Ge are present within the first coordination spheres of each other. These results directly demonstrate, through complementary spectroscopic analysis and atomically resolved STEM imaging, that the Re–Ge nanoparticles form random alloys with a unique FCCf crystal structure. Although the present results of this study do not allow a clear distinction between the individual contributions of electronic effects (the electron-rich Re(0) state) and geometric effects (the shortened bond distances, the FCCf structure and random alloy mixing), both are likely to play important roles in the enhanced catalytic performance.

Conclusions

This study focused on Re–Ge catalysts, which exhibit excellent activity and selectivity for the direct hydrogenation of carboxylic acids. The aim was to elucidate the changes in structural and electronic state occurring during the preparation steps and thereby identify the key structural factors responsible for the high catalytic performance. To this end, a complementary approach combining *in situ* XAFS and *ex situ* STEM was employed. The results revealed that the highly active catalytic state is associaed with approximately 1 nm crystalline nanoparticles formed during the hydrogen reduction step. The unique crystal structure of the nanoparticles was identified as the low-energy FCCf structure, based on DFT calculations. Furthermore, Re and Ge mixed at the atomic level to form a random alloy within the nanoparticles. This alloy formation stabilized the metallic Re(0) state, rendering Re electron-rich. Although the present results do not allow a clear distinction between the individual contributions of electronic and geometric effects, both are likely to play important roles in the

high catalytic performance. It was also found that the performance degradation accompanying the oxidative stabilization step was attributable not to changes in particle size or dispersion but to the re-oxidation of Ge within the nanoparticles, as revealed by the increased Ge–O coordination number detected by XAFS and the consequent loss of crystallinity observed by STEM. This close correlation between the changes in the chemical state and the physical structure highlights the critical importance of preserving the reduced Re–Ge alloy phase for maintaining high catalytic performance. This study not only elucidated the high-performance mechanism but also demonstrated the importance of stabilizing the unique metastable nanoscale phases and the resulting beneficial electronic interactions between the constituent elements. The present approach for directly linking spatially-averaged chemical state changes obtained by XAFS with the atomic-scale structural changes of individual nanoparticles revealed by STEM provides an effective strategy for identifying the performance-determining factors in complex nanomaterial systems, thereby facilitating the rational design of high-performance catalysts.

Author contributions

M. S., R. S., Y. I. and T. M. proposed the project and designed the experiments. R. S., Y. I., and T. M. developed the Re–Ge/TiO_2 catalyst. Y. I. collected the *in situ* XAFS data and R. S. was responsible for the in-depth XAFS/EXAFS data analysis and interpretation. M. S. performed the *ex situ* and HAADF-STEM observations and related software-based image analysis. Y. F. conducted the DFT calculations and contributed to structural model visualization. T. M., R. S., and H. M. acquired funding and provided resources. K. M. and A. H. supervised the project and managed project administration. M. S. and R. S. co-wrote the manuscript and co-led the manuscript revision and he response to the reviewers, with contributions from all authors.

Conflicts of interest

There are no conflicts to declare.

Data availability

The data supporting this article have been included as part of the supplementary information (SI). Supplementary information: figures and tables for material characterization. See DOI: https://doi.org/10.1039/d5nr05414a.

Acknowledgements

We thank Mr Y. Kikuchi (MCC) and Mr H. Yamanaka (MCC) for performing the XRD measurements, Dr K. Okamoto (MCC) for providing valuable support with the *in situ* XAFS measurements, and Prof. Anatoly Frenkel (SBU) and Dr Ramsey Salcedo (GC, CUNY) for providing the reference spectra for the XAFS analysis. This study was partially supported by the "Advanced Research Infrastructure for Materials and Nanotechnology in Japan (ARIM)", Department of the Ministry of Education, Culture, Sports, Science, and Technology (MEXT) (Grant Number JPMXP1224NM5123), by KAKENHI, the Japan Society for the Promotion of Science (Grant Number 24K15598, K. M.) and by Precursory Research for Embryonic Science and Technology (PRESTO), JST (Grant Number JPMJPR17S7, A. H.). We thank Edanz (https://jp.edanz.com/ac) for editing a draft of this manuscript.

References

1 R. Ferrando, J. Jellinek and R. L. Johnston, *Chem. Rev.*, 2008, **108**, 845–910.
2 K. D. Gilroy, A. Ruditskiy, H.-C. Peng, D. Qin and Y. Xia, *Chem. Rev.*, 2016, **116**, 10414–10472.
3 D. Wang, H. L. Xin, R. Hovden, H. Wang, Y. Yu, D. A. Muller, F. J. DiSalvo and H. D. Abruña, *Nat. Mater.*, 2013, **12**, 81–87.
4 V. R. Stamenkovic, B. S. Mun, M. Arenz, K. J. J. Mayrhofer, C. A. Lucas, G. Wang, P. N. Ross and N. M. Markovic, *Nat. Mater.*, 2007, **6**, 241–247.
5 M. L. Gothe, K. L. C. Silva, A. L. Figueredo, J. L. Fiorio, J. Rozendo, B. Manduca, V. Simizu, R. S. Freire, M. A. S. Garcia and P. Vidinha, *Eur. J. Inorg. Chem.*, 2021, **2021**, 4043–4065.
6 J. S. Reinhold, J. Pang, B. Zhang, F. E. Kühn and T. Zhang, *Green Chem.*, 2024, **26**, 10661–10686.
7 J. Luo and C. Liang, *ACS Catal.*, 2024, **14**, 7032–7049.
8 B. Rozmysłowicz, A. Kirilin, A. Aho, H. Manyar, C. Hardacre, J. Wärnå, T. Salmi and D. Yu. Murzin, *J. Catal.*, 2015, **328**, 197–207.
9 T. Toyao, S. M. A. H. Siddiki, A. S. Touchy, W. Onodera, K. Kon, Y. Morita, T. Kamachi, K. Yoshizawa and K. Shimizu, *Chem. – Eur. J.*, 2017, **23**, 1001–1006.
10 M. L. Gothe, A. H. Braga, L. R. Borges, J. Hong, G. Farias, A. D. T. Baptista, B. A. L. Larico, A. B. M. Cansian, C. R. Miranda, S. R. Bare, L. M. Rossi and P. Vidinha, *ACS Catal.*, 2025, 19111–19126.
11 Y. Takeda, M. Tamura, Y. Nakagawa, K. Okumura and K. Tomishige, *ACS Catal.*, 2015, **5**, 7034–7047.
12 K. H. Kang, U. G. Hong, Y. Bang, J. H. Choi, J. K. Kim, J. K. Lee, S. J. Han and I. K. Song, *Appl. Catal., A*, 2015, **490**, 153–162.
13 X. Cao, J. Zhao, F. Long, P. Liu, X. Jiang, X. Zhang, J. Xu and J. Jiang, *Appl. Catal., B*, 2022, **312**, 121437.
14 A. Suknev, V. Zaikovskii, V. Kaichev, E. Paukshtis, E. Sadovskaya and B. Bal'zhinimaev, *J. Energy Chem.*, 2015, **24**, 646–654.
15 X. Huang, K. Liu, W. L. Vrijburg, X. Ouyang, A. I. Dugulan, Y. Liu, M. W. G. M. T. Verhoeven, N. A. Kosinov, E. A. Pidko and E. J. M. Hensen, *Appl. Catal., B*, 2020, **278**, 119314.
16 Y. Inami, T. Matsuo, R. Shimogawa and T. Aoshima, The 9th Tokyo Conference on Advanced Catalytic Science and Technology (TOCAT9), Fukuoka, Japan.

17 Y. Inami, R. Shimogawa, T. Matsuo and M. Shimizu, *Mitsubishi Chemical corporation Pat* P2025-133481A, 2025.
18 Y.-L. Sun, Y.-L. Deng, H.-N. Chen, X.-T. Yang, X.-M. Lin and J.-F. Li, *Small Struct.*, 2023, **4**, 2200201.
19 E. Groppo, S. Rojas-Buzo and S. Bordiga, *Chem. Rev.*, 2023, **123**, 12135–12169.
20 A. A. Herzing, C. J. Kiely, A. F. Carley, P. Landon and G. J. Hutchings, *Science*, 2008, **321**, 1331–1335.
21 E. I. Ross-Medgaarden, W. V. Knowles, T. Kim, M. S. Wong, W. Zhou, C. J. Kiely and I. E. Wachs, *J. Catal.*, 2008, **256**, 108–125.
22 D. S. Su, B. Zhang and R. Schlögl, *Chem. Rev.*, 2015, **115**, 2818–2882.
23 A. K. Datye, *J. Catal.*, 2003, **216**, 144–154.
24 J.-D. Grunwaldt, J. B. Wagner and R. E. Dunin-Borkowski, *ChemCatChem*, 2013, **5**, 62–80.
25 S. W. Chee, T. Lunkenbein, R. Schlögl and B. R. Cuenya, *Chem. Rev.*, 2023, **123**, 13374–13418.
26 J. M. Thomas, C. Ducati, R. Leary and P. A. Midgley, *ChemCatChem*, 2013, **5**, 2560–2579.
27 J. Qu, M. Sui and R. Li, *iScience*, 2023, **26**, 107072.
28 B. He, Y. Zhang, X. Liu and L. Chen, *ChemCatChem*, 2020, **12**, 1853–1872.
29 M. Newville, *J. Phys.: Conf. Ser.*, 2013, **430**, 012007.
30 M. J. Piotrowski, C. G. Ungureanu, P. Tereshchuk, K. E. A. Batista, A. S. Chaves, D. Guedes-Sobrinho and J. L. F. Da Silva, *J. Phys. Chem. C*, 2016, **120**, 28844–28856.
31 P. Giannozzi, S. Baroni, N. Bonini, M. Calandra, R. Car, C. Cavazzoni, D. Ceresoli, G. L. Chiarotti, M. Cococcioni, I. Dabo, A. Dal Corso, S. de Gironcoli, S. Fabris, G. Fratesi, R. Gebauer, U. Gerstmann, C. Gougoussis, A. Kokalj, M. Lazzeri, L. Martin-Samos, N. Marzari, F. Mauri, R. Mazzarello, S. Paolini, A. Pasquarello, L. Paulatto, C. Sbraccia, S. Scandolo, G. Sclauzero, A. P. Seitsonen, A. Smogunov, P. Umari and R. M. Wentzcovitch, *J. Phys.: Condens. Matter*, 2009, **21**, 395502.
32 P. E. Blöchl, *Phys. Rev. B: Condens. Matter Mater. Phys.*, 1994, **50**, 17953–17979.
33 G. Kresse and D. Joubert, *Phys. Rev. B: Condens. Matter Mater. Phys.*, 1999, **59**, 1758–1775.
34 J. P. Perdew, K. Burke and M. Ernzerhof, *Phys. Rev. Lett.*, 1996, **77**, 3865–3868.
35 J. Madsen and T. Susi, *Open Res. Eur.*, 2021, **1**, 24.
36 T. Matsuo, Y. Yoshikawa and T. Aoshima, *Mitsubishi Chemical corporation Pat* JP7111093B2, 2022.
37 J. Zhao, L. Yang, J. A. McLeod and L. Liu, *Sci. Rep.*, 2015, **5**, 17779.
38 A. Genc, J. Marlowe, A. Jalil, D. Belzberg, L. Kovarik and P. Christopher, *Ultramicroscopy*, 2025, **271**, 114116.
39 T. Siegrist, F. Hulliger and W. Petter, *J. Less-Common Met.*, 1983, **90**, 143–151.
40 A. Rabus and E. Mun, *Phys. Rev. Mater.*, 2019, **3**, 013404.
41 S. Gražulis, A. Daškevič, A. Merkys, D. Chateigner, L. Lutterotti, M. Quirós, N. R. Serebryanaya, P. Moeck, R. T. Downs and A. Le Bail, *Nucleic Acids Res.*, 2012, **40**, D420–D427.
42 T. Rapps, R. Ahlrichs, E. Waldt, M. M. Kappes and D. Schooss, *Angew. Chem., Int. Ed.*, 2013, **52**, 6102–6105.
43 S. J. Pennycook and D. E. Jesson, *Ultramicroscopy*, 1991, **37**, 14–38.
44 P. D. Nellist and S. J. Pennycook, *Ultramicroscopy*, 1999, **78**, 111–124.
45 R. F. Loane, P. Xu and J. Silcox, *Acta Crystallogr., Sect. A: Found. Crystallogr.*, 1991, **47**, 267–278.